Gravity-driven Magnetic Field at ∼1000 au Scales in High-mass Star Formation

Patricio Sanhueza[1,2] , Josep Miquel Girart[3,4] , Marco Padovani[5] , Daniele Galli[5] , Charles L. H. Hull[6,7,20] ,
Qizhou Zhang[8] , Paulo Cortes[9] , Ian W. Stephens[10] , Manuel Fernández-López[11] , James M. Jackson[12] , Pau Frau[13],
Patrick M. Koch[14] , Benjamin Wu[15,1] , Luis A. Zapata[16] , Fernando Olguin[17] , Xing Lu[1] , Andrea Silva[18,1] ,
Ya-Wen Tang[14] , Takeshi Sakai[19] , Andrés E. Guzmán[1] , Ken'ichi Tatematsu[1,2] , Fumitaka Nakamura[1,2] , and
Huei-Ru Vivien Chen[17]

[1] National Astronomical Observatory of Japan, National Institutes of Natural Sciences, 2-21-1 Osawa, Mitaka, Tokyo 181-8588, Japan; patricio.sanhueza@nao.ac.jp
[2] Department of Astronomical Science, SOKENDAI (The Graduate University for Advanced Studies), 2-21-1 Osawa, Mitaka, Tokyo 181-8588, Japan
[3] Institut de Ciencies de l'Espai (ICE, CSIC), Can Magrans s/n, E-08193, Cerdanyola del Vallès, Catalonia, Spain
[4] Institut d'Estudis Espacials de Catalunya (IEEC), E-08034, Barcelona, Catalonia, Spain
[5] INAF-Osservatorio Astrofisico di Arcetri, Largo E. Fermi 5, I-50125 Firenze, Italy
[6] National Astronomical Observatory of Japan, Alonso de Córdova 3788, Office 61B, 7630422, Vitacura, Santiago, Chile
[7] Joint ALMA Observatory, Alonso de Córdova 3107, Vitacura, Santiago, Chile
[8] Center for Astrophysics | Harvard & Smithsonian, 60 Garden Street, Cambridge, MA 02138, USA
[9] National Radio Astronomy Observatory, 520 Edgemont Road, Charlottesville, VA 22903, USA
[10] Department of Earth, Environment and Physics, Worcester State University, Worcester, MA 01602, USA
[11] Instituto Argentino de Radioastronomía (CCT-La Plata, CONICET; CICPBA), C.C. No. 5, 1894, Villa Elisa, Buenos Aires, Argentina
[12] USRA SOFIA Science Center, NASA Ames Research Center, Moffett Field, CA 94045, USA
[13] Private Researcher
[14] Academia Sinica Institute of Astronomy and Astrophysics, 11F of Astro-Math Bldg, 1, Section 4, Roosevelt Road, Taipei 10617, Taiwan
[15] NVIDIA Research, 2788 San Tomas Expressway, Santa Clara, CA 95051, USA
[16] Instituto de Radioastronomía y Astrofísica, Universidad Nacional Autónoma de México, P.O. Box 3-72, 58090, Morelia, Michoacán, Mexico
[17] Institute of Astronomy and Department of Physics, National Tsing Hua University, Hsinchu 30013, Taiwan
[18] Kavli Institute for the Physics and Mathematics of the Universe, The University of Tokyo, Kashiwa 277-8583, Japan
[19] Graduate School of Informatics and Engineering, The University of Electro-Communications, Chofu, Tokyo 182-8585, Japan

Abstract

A full understanding of high-mass star formation requires the study of one of the most elusive components of the energy balance in the interstellar medium: magnetic fields. We report Atacama Large Millimeter/submillimeter Array (ALMA) 1.2 mm, high-resolution (700 au) dust polarization and molecular line observations of the rotating hot molecular core embedded in the high-mass star-forming region IRAS 18089−1732. The dust continuum emission and magnetic field morphology present spiral-like features resembling a whirlpool. The velocity field traced by the $H^{13}CO^+$ ($J = 3−2$) transition line reveals a complex structure with spiral filaments that are likely infalling and rotating, dragging the field with them. We have modeled the magnetic field and find that the best model corresponds to a weakly magnetized core with a mass-to-magnetic-flux ratio (λ) of 8.38. The modeled magnetic field is dominated by a poloidal component, but with an important contribution from the toroidal component that has a magnitude of 30% of the poloidal component. Using the Davis–Chandrasekhar–Fermi method, we estimate a magnetic field strength of 3.5 mG. At the spatial scales accessible to ALMA, an analysis of the energy balance of the system indicates that gravity overwhelms turbulence, rotation, and the magnetic field. We show that high-mass star formation can occur in weakly magnetized environments, with gravity taking the dominant role.

1. Introduction

High-mass stars dominate the energy input and chemical enrichment of galaxies. Among all the ingredients that have to be considered in their formation, the magnetic field is by far the least explored. Indeed, it is still debated how the magnetic energy compares to other energies in play, namely, turbulence, gravity, and rotation.

Observations of linearly polarized dust emission are currently the best available tool to infer the magnetic field in molecular clouds and denser regions associated with star formation (e.g., Hull & Zhang 2019). Dust polarization observations of high-mass star-forming regions suggest that the magnetic field appears to be dynamically important during the collapse and fragmentation of parsec-scale molecular clumps and the mass assembly of dense cores at scales of 0.01–0.1 pc (Zhang et al. 2014; Hull & Zhang 2019; Cortes et al. 2019). However, it remains unclear whether at smaller scales (core–disk interface, ∼1000 au) the star formation process is magnetically dominated (Girart et al. 2009; Beltrán et al. 2019; Beuther et al. 2020; Cortes et al. 2021; Fernández-López et al. 2021). So far, since polarization observations are scarce at these small scales, it is difficult to evaluate the overall importance of the magnetic field in the high-mass star formation process.

Located at a parallax distance of 2.34 kpc (Xu et al. 2011) with a bolometric luminosity of $1.3 \times 10^4 \, L_{\odot}$ (Sridharan et al. 2002), the high-mass star-forming region IRAS 18089−1732 is an ideal laboratory to assess the importance of the magnetic field with respect to turbulence, gravity, and rotation. Earlier studies at arcsec resolution show that IRAS 18089−1732 has a

deeply embedded hot core (Beuther et al. 2004a, 2004b) and a disk-like rotating structure roughly perpendicular to a molecular outflow. A line-of-sight magnetic field strength of 8.4 and 5.5 mG has been estimated from measurements of Zeeman splitting of the 6.7 GHz CH_3OH maser line using the 100 m Effelsberg telescope (Vlemmings 2008) and the MultiElement Radio Linked Interferometer Network (MERLIN; Dall'Olio et al. 2017), respectively. Early observations of IRAS 18089 −1732 with the Submillimeter Array (SMA) show the detection of at least a few independent polarization measurements in dust continuum emission (Beuther et al. 2010). Taking advantage of the superlative capabilities of the Atacama Large Millimeter/submillimeter Array (ALMA), we have observed IRAS 18089−1732 in polarized dust continuum and molecular line emission to better understand the role of the magnetic field in the formation of high-mass stars. This target was observed as part of the Magnetic fields in Massive star-forming Regions (MagMaR) survey that in total contains 30 sources. Details on the survey and source selection will be given in P. Sanhueza et al. (2021, in preparation). Early results on two high-mass star-forming regions, G5.89-0.39 and NGC 6334I(N), are presented in Fernández-López et al. (2021) and Cortes et al. (2021), respectively.

2. Observations

ALMA polarization observations (Project ID: 2017.1.00101. S; PI: Sanhueza) of IRAS 18089−1732 were taken on 2018 September 25. A total of 47 antennas of the 12 m array were used, covering baselines from 15 to 1400 m that resulted in an angular resolution of $\sim$0″3. The data set consists of full polarization observations in Band 6 ($\sim$250.486 GHz; 1.2 mm). The correlator setup includes three spectral windows of width 1875 MHz, with a spectral resolution of 1.95 MHz ($\sim$2.4 km s^{-1}), and two spectral windows of width 234 MHz, with a spectral resolution of 0.488 MHz (0.56 km s^{-1}).

Linearly polarized dust continuum emission is detected in the inner $\sim$8″ of the observed field, the inner one-third of the primary beam (24″), with polarization angles having less than 1% errors. We note, however, that polarization angles on angular scales up to the width of the primary beam have only few percent errors (Hull et al. 2020). Line contamination was removed from the continuum (Stokes I) image following the procedure described in Olguin et al. (2021). Stokes I was self-calibrated in phase and amplitude, while Stokes Q and U were only self-calibrated in phase. Self-calibration solutions were then applied to the spectral cubes.

The continuum imaging was done by independently cleaning each Stokes parameter using the CASA task *tclean* with Briggs weighting and robust parameter of 1. The resulting images have an angular resolution of 0″27 × 0″34 and sensitivities of 175 μJy beam^{-1} for Stokes I and 31.4 μJy beam^{-1} for both Stokes Q and U. The polarized intensity image was debiased following Vaillancourt (2006). The peak of the polarized dust emission is 1.4 mJy beam^{-1}. The mean (median) polarization fraction is 5% (4%).

The $H^{13}CO^+$ line emission was imaged using the automatic masking procedure *yclean* from Contreras et al. (2018). The CASA task *tclean* with Briggs weighting and robust parameter of 1 was used, resulting in a noise level of 3.2 mJy beam^{-1} per 0.56 km s^{-1} channel.

The quasar J1924–2914 was used for the calibration of flux, bandpass, and polarization. The quasar J1832–2039 was used for phase calibration. Data calibration and imaging were performed using CASA 5.1.1 and 5.5.0, respectively.

3. Results

The ALMA observations at 1.2 mm with a spatial resolution of 700 au (0″3) allow us to observe the internal structure of IRAS 18089−1732 in great detail (Figure 1). The dust continuum emission peaks at the position of the previously reported hot core (Beuther et al. 2004a, 2004b; Zapata et al. 2006). The overall emission is asymmetric, with an extension toward the northwest of the brightest 1.2 mm peak. In addition, there are spiral-like streamers associated with the central hot core having a counterclockwise orientation (mimicking a whirlpool). The magnetic field projected in the plane of the sky also traces spiral-like features connected to the central hot core, roughly following the dusty spirals and making more evident the whirlpool shape (Figure 1).

Along with the continuum emission, there are myriad molecular line transitions detected with different excitation conditions (i.e., tracing different temperature and density regimes). Among these, here we focus on $H^{13}CO^+$ ($J = 3-2$) and leave the tracers of the inner hot core for a forthcoming work (V. Chen et al. 2021, in preparation). The emission from the $H^{13}CO^+$ ($J = 3-2$) line shows a spatial distribution coincident with that of the dust emission, as can be seen in the integrated intensity map (Figure 2(a)). This molecule is a good tracer of the relatively cold ($E_u = 25$ K), dense material in the spiral-like and filamentary structures found in IRAS 18089−1732. The $H^{13}CO^+$ spectra show two clear velocity components separated by $\sim$4 km s^{-1} that can be traced continuously from the regions in which they overlap (presenting double-line profiles) to regions where only a single component is detected. To properly trace the velocity field of both components, a simultaneous Gaussian fitting of both velocity components was performed. Figure 2(b) shows the velocity field traced by the blueshifted gas component (with respect to the systemic cloud velocity $v_{LSR} \approx 33.0$ km s^{-1}), while Figure 2(c) shows the velocity field traced by the redshifted gas component. Near the center of the hot core, the $H^{13}CO^+$ profile becomes complex, exhibiting extremely broad line widths, absorption features, and blending with hot core lines, precluding a successful Gaussian fitting.

A prominent spiral-like feature in the blueshifted gas component that follows the magnetic field morphology is seen in Figure 2(b). Although there is significant substructure in the velocity pattern along this spiral-like filament, it has an overall velocity difference of $\sim$1.4 km s^{-1} over a length of 7.3″ (17000 au), resulting in a 17 km s^{-1} pc^{-1} velocity gradient. The redshifted gas component shows two filaments that coincide with the area emitting polarized emission (Figure 2(c)), one extending to the north and the other one to the south of the central hot core. The northern filament starts at 3″3 (7700 au) from the hot core with blueshifted velocities of $\sim$34.1 km s^{-1} and then connects to the red side of the rotating central hot core at $\sim$36.1 km s^{-1} (velocity gradient of 53.6 km s^{-1} pc^{-1}). The southern filament extends over 2″9 (6800 au) with extreme velocities of $\sim$34.2 and $\sim$36 km s^{-1}, resulting in a velocity gradient of 54.6 km s^{-1} pc^{-1}. In the position–position–velocity (PPV) space displayed in Figure 3, the distribution of the gas and the main structures, spiral and northern/southern filaments, can be seen. Figure 3(a) simultaneously displays both the blueshifted and redshifted velocity components and is comparable to displaying Figures 2(b) and (c) in a single image. Figures 3(b)
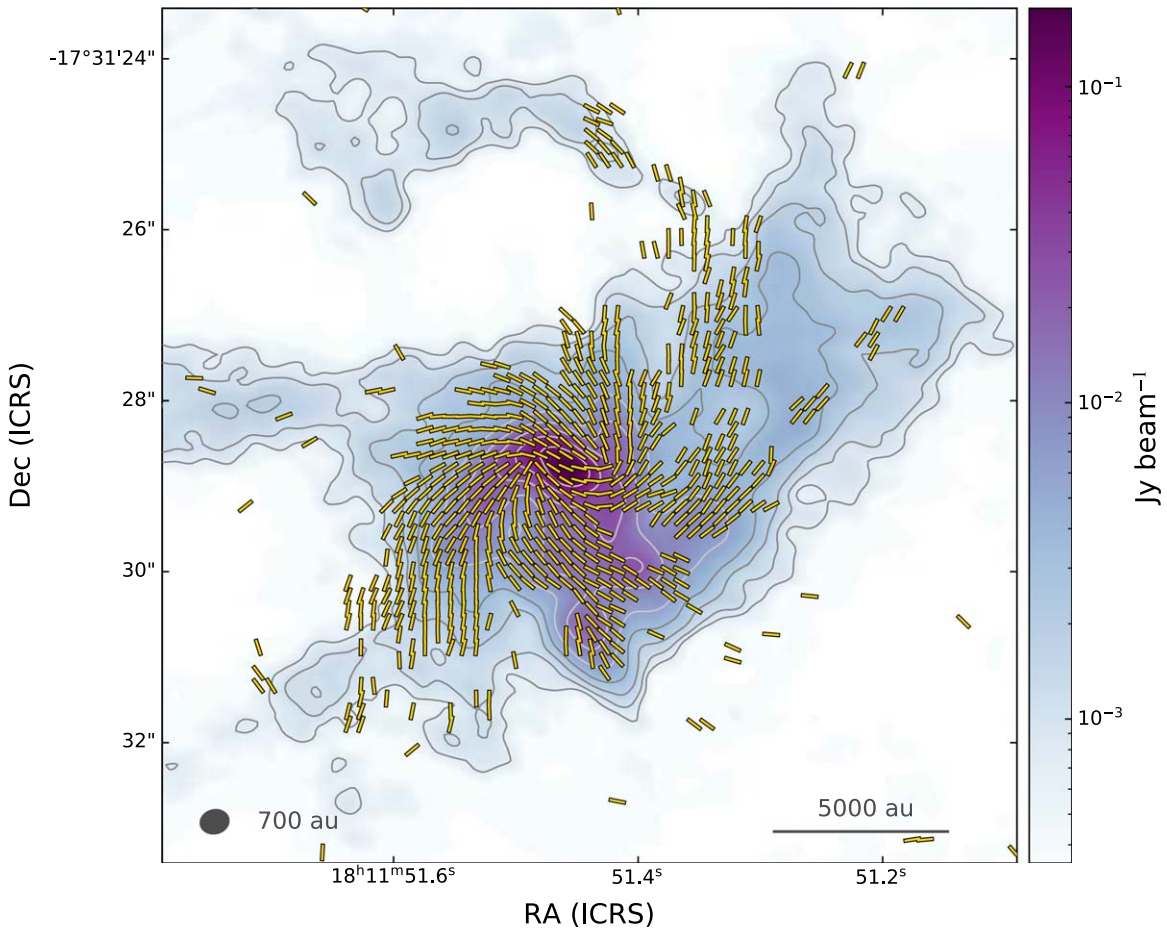
Figure 1. ALMA 1.2 mm dust continuum emission (color scale and contours) toward IRAS 18089−1732 with overlaid magnetic field vectors, which correspond to the dust polarization vectors rotated by 90°. Yellow line segments representing the magnetic field orientation are plotted above the 3σ level, with $\sigma = 31.4$ μJy beam^{-1}, and have an arbitrary length. Contours correspond to the dust continuum emission in steps of 4, 6, 10, 18, 34, 66, 130, 258, and 514 times the σ (rms) value of 175 μJy beam^{-1}. Spatial resolution of 700 au (0$\farcs$3) is shown on the bottom left. Scale bar is shown on the bottom right side of the panel.

and (c) show the three main structures from different angles. Figure 3(d) corresponds to a position–velocity (PV) diagram. Figure 3(d) shows, at the positions indicated by the black arrows, how the velocity increases closer to the central hot core, especially in the southern and northern filaments. Such an increase in velocity is typical of gas accelerating close to the central object and is a sign of infall (Tobin et al. 2012).

4. Discussion

4.1. Dust Continuum Emission

The physical properties of the central region of IRAS 18089−1732 were calculated in the area enclosed by the 10σ contour, which has a flux density of 1.38 Jy. We choose to analyze this area because it includes most of the polarized emission and excludes the most diffuse material and the outflow cavity (see Beuther et al. 2004a). Assuming optically thin dust emission, the total gas mass enclosed in the main dust structure is 75 $M_\odot$ (Appendix A). The average number density is 1.3×10^7 cm^{-3}, resulting in a free-fall time of 8.4×10^3 yr.

4.2. Line Emission and Accretion Flows

The spiral-feature and filaments seen in H^{13}CO$^+$ (Figure 2) resemble the accretion flows funneling material to disk scales that have been observed (also using high angular resolution

observations) in a few other high-mass star-forming regions (e.g., Liu et al. 2015; Maud et al. 2017; Izquierdo et al. 2018; Goddi et al. 2020). Following standard procedures, we convert the H^{13}CO$^+$ emission tracing the blueshifted spiral-feature and redshifted filaments into total gas mass (Appendix B).

The spiral-feature has a gas mass of 2.2 $M_\odot$, while the northern and southern filaments have 1.4 and 0.60 $M_\odot$, respectively. If the velocity gradients observed are produced by material flowing toward the inner hot core, we estimate a combined infall rate of 0.9–2.5 $\times 10^{-4}$ $M_\odot$ yr^{-1} for inclination angles between 30° and 60°, larger than the accretion rates through filaments seen in other high-mass star-forming regions at larger scales (Lu et al. 2018). These infall rates imply that the central disk-like structure can be replenished with 0.70–2.1 $M_\odot$ per free-fall time (8.4×10^3 yr), thus contributing to the increase in the mass of the central high-mass star.

4.3. Modeling the Magnetic Field

To model the polarization pattern observed in IRAS 18089−1732, we used the *DustPol* module contained in the ARTIST package (Padovani et al. 2012) and followed the same procedure described in Beltrán et al. (2019). We then perform synthetic ALMA observations of the models and compare the resulting polarization position angles with the observations. *DustPol* creates a set of FITS images related to the Stokes
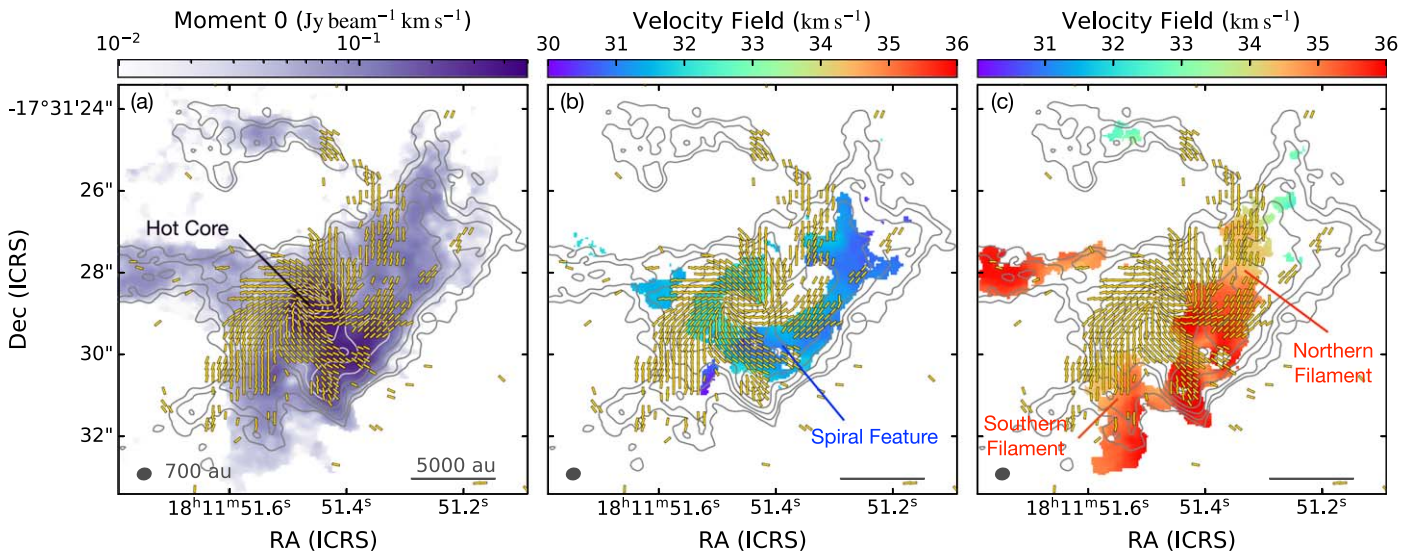
Figure 2. H^{13}CO$^+$ integrated intensity (moment 0) in panel (a) and velocity fields in panels (b) and (c). Yellow vectors, of an arbitrary length, indicate the inferred magnetic field and gray contours show the dust continuum emission (same as Figure 1). In (a), the moment 0 includes both velocity components. In (b), the blueshifted component has a spiral-like shape following the magnetic field with a velocity gradient of 17 km s^{-1} pc^{-1}. In (c), the redshifted gas component shows two filaments that follow the magnetic field with velocity gradients of ~54 km s^{-1} pc^{-1}.
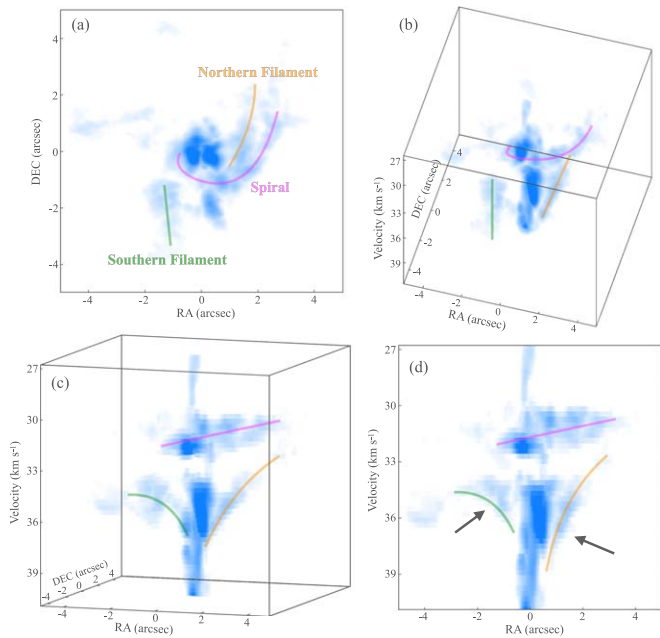

Figure 3. Selected views of the position–position–velocity (PPV) distribution of the H^{13}CO$^+$ emission. (a) View in position–position (PP) space, comparable to combining Figures 2(b) and (c) into a single image. The main structures in IRAS 18089−1732 are delineated and labeled. (b) and (c) PPV distribution from different angles, with the position of the main features marked. (d) View of the position–velocity (PV) space with the main structures marked. Arrows point to the places where the gas is accelerating and infalling toward the central source.

parameters (I, Q, U) that is directly used as an input for the CASA simobserve/simanalyze tasks, which use the same antenna configuration of the observing runs.

The model used for the magnetic field configuration is an axisymmetric singular toroid threaded by an hourglass-shaped poloidal field (Li & Shu 1996; Padovani & Galli 2011) with an added toroidal component to mimic the effect of rotation as in Padovani et al. (2013). More details on the model are given in

Appendix C. The main purpose of the modeling is to determine basic properties of the magnetic field (mass-to-magnetic-flux ratio, toroidal-to-poloidal ratio, inclination) to be compared with observations, and to provide the configuration of the mean field needed to perform the Davis–Chandrasekhar–Fermi (DCF; Davis 1951; Chandrasekhar & Fermi 1953) analysis of the polarization angle residuals.

We performed a χ^2 test for all the combinations of the parameters λ, b_0, and i and found that the set $\lambda = 8.38$, $b_0 = 0.30^{+0.28}_{-0.18}$, and $i = -5^{+25°}_{-15}$ gives the lowest reduced χ^2 value ($\bar{\chi}^2 = 4.13$). The magnetic field is dominated by a poloidal component, but with an important contribution from the toroidal component, whose magnitude is 30% of the poloidal component. This significant contribution from the toroidal component indicates that rotation is affecting the magnetic field. Figure 4, shows the comparison between the observed and modeled polarization angles. The excellent agreement is shown quantitatively in the inset of the same figure. The latter illustrates the distribution of the polarization angle residuals, $\Delta\psi = \psi_{obs} - \psi_{mod}$, defined as the difference between the observed (ψ_{obs}) and modeled (ψ_{mod}) polarization angles, whose Gaussian fit gives a mean value of $\langle\Delta\psi\rangle = 1°.15$ and a standard deviation $\sigma_\psi = 18°.09$. The latter is needed for the DCF method. The λ value of 8.38 of the best model characterizes the mass inside a flux tube, while observationally the mass is estimated assuming a spherical source. To correct for this, λ must be divided by a correction factor of 2.32 (Li & Shu 1996), leading to an effective λ of 3.61. Despite the relative simplicity of the model, this value of λ is very close to that estimated from observations (see Section 4.4). It should be stressed that cloud models with smaller values of λ cannot be completely ruled out. For example, a model with $\lambda = 2.66$ also provides an acceptable fit to the data, resulting in $b_0 = 0.40^{+0.50}_{-0.21}$ and $i = 0^{+22°}_{-22}$ with a slightly worse value of $\bar{\chi}^2 = 4.65$ (for smaller values of λ, the $\bar{\chi}^2$ becomes progressively larger). We note that the magnetic field strength determined in the following section would not change adopting the $\lambda = 2.66$ model because its $\sigma_\psi = 18°.52$ practically has the same value (18°.09) as in the preferred $\lambda = 8.38$ model.
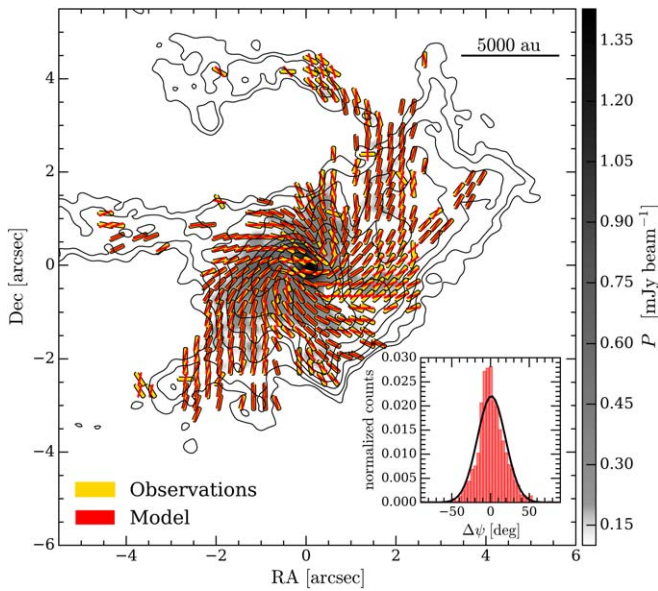
Figure 4. Observed polarization angles showing the magnetic field orientation (yellow segments) on top of which are superposed those obtained from the best-fit model ($\lambda = 8.38$, $b_0 = 0.30^{+0.28}_{-0.18}$, and $i = -5^{+25°}_{-15}$; red segments). The black contours show the dust continuum emission (same as Figure 1), and the gray-scale map displays the polarized intensity, P. Scale bar is shown on the top right side of the panel. The inset shows the histogram of the polarization angle residuals $\Delta\psi = \psi_{\rm obs} - \psi_{\rm mod}$ with its Gaussian fit (black line).

4.4. Analysis of the Energy Balance

To estimate the magnetic field strength, we employ the DCF method, calculating the dispersion of the difference between the observed and modeled polarization angles (Appendix D). The estimated magnetic field strength and Alfvén speed are 3.5 mG and 1.26 km s^{-1}, respectively.

Once the magnetic field strength is estimated, we can assess the importance of each energy component involved in the star formation process in IRAS 18089−1732. To put things into context, previous observations find that at low densities and large scales (a few to several parsecs), the magnetic field tends to be parallel to filamentary gas structures (e.g., Clark et al. 2014; Planck Collaboration et al. 2016), which in some cases has been interpreted as material being funneled by the magnetic field toward the cloud center (Palmeirim et al. 2013). On the other hand, at higher densities and smaller scales (∼0.5–1 pc), the magnetic field is typically found perpendicular to the gas structures (e.g., Zhang et al. 2014; Planck Collaboration et al. 2016; Soler et al. 2017; Liu et al. 2018; Juvela et al. 2018; Fissel et al. 2019; Soam et al. 2019). At scales of a few thousand astronomical units (a few times 0.001 pc), however, the relationship between field direction and gas structures is much more uncertain. In IRAS 18089−1732, the magnetic field morphology has a spiral pattern at scales from 0.1 pc down to 0.003 pc. The magnetic field vectors tend to follow the spiral-like features and filaments seen in both the continuum as well as in the molecular line emission. As suggested by the model, the twisted morphology of the magnetic field seems to be produced by gas rotating around the hot core.

To confirm if gravity has overwhelmed the support that the magnetic field can provide against collapse, we calculate the mass-to-magnetic-flux ratio (λ; Appendices C and D). From observations, we obtain a λ of 3.2 (consistent with the model value mentioned above after correcting for geometry),

indicating that the core is supercritical and likely collapsing. Indeed, the magnetic to gravitational energy ratio is 0.11. Turbulence is an additional source of energy that can oppose gravity, and in low-mass star-forming regions, turbulence has been found to be more dynamically important than the magnetic field (Hull et al. 2017). Their relative importance can be assessed by the turbulence-to-magnetic-energy ratio, β_t. We obtain a β_t of 1.1, which indicates that turbulence and the magnetic field play a comparable role in supporting the IRAS 18089−1732 core against collapse. With an excellent agreement between the observations and the model seen in Figure 4, the important contribution from the toroidal component of the magnetic field reveals the effects of rotation, suggesting that the rotational and magnetic field energy should be comparable. We estimate the rotational energy of the system (Appendix D) and find that it is also overcome by the gravitational energy and it is only slightly weaker than the magnetic field energy. To assess the relative importance of all energies at play, the virial analysis is frequently performed. In its basic form, the virial analysis includes only gravity and turbulence, and relies on the determination of the virial parameter ($\alpha_{\rm vir}$). We computed a virial parameter of 0.24 (unity indicates equilibrium), which indicates collapse. The overwhelming importance of gravity with respect to the other energies becomes more evident once we include the magnetic field and rotation. After adding the magnetic field and then rotation, we obtain virial parameters of 0.35 ($\alpha_{\rm vir,B}$) and 0.57 ($\alpha_{\rm vir,B,rot}$; see derivation in Appendix D), respectively. These calculations of the virial parameter assume a uniform density profile. If a centrally peaked density profile is used, virial parameters are 50%–60% smaller: 0.14 ($\alpha_{\rm vir}$), 0.21 ($\alpha_{\rm vir,B}$), and 0.28 ($\alpha_{\rm vir,B,rot}$), diminishing the importance of other energies with respect to gravity.

Overall, at the scales we observe in IRAS 18089−1732, the magnetic field morphology seems to be dictated by dynamical processes such as inflow and rotation, thus indicating a diminished importance of the magnetic field at the current evolutionary stage. The analysis of the energies in play supports that gravity has taken the dominant role in the immediate vicinity (∼1000 au scales) of a high-mass star in formation, and the magnetic field importance is only comparable to turbulence and rotation.

5. Conclusions

ALMA observations of the high-mass star-forming region IRAS 18089−1732 have revealed that the dense molecular envelope surrounding the high-mass star has a complex spiral pattern at the 0.003–0.1 pc scales. This spiral-like morphology is seen in the gas and dust (traced by the H^{13}CO$^+$ ($J = 3-2$) line and the 1.2 mm continuum emission, respectively), as well as in the magnetic field (traced by the linearly polarized 1.2 mm dust emission). At the observed size scales, gravitational infall clearly dominates over the support from the magnetic field, turbulence, and rotation, resulting in the feeding of the inner dense, hot circumstellar disk-like structure with a high accretion rate of $0.9-2.5 \times 10^{-4}$ $M_\odot$ yr^{-1}. We show that high-mass star formation can occur in weakly magnetized environments and that gravity is shaping the immediate surrounding around the high-mass star. The spiral magnetic field indicates that angular momentum is high enough to twist the field lines, as supported by the model and the energy analysis. With these observations and consistent with previous works in other high-mass star-forming regions (e.g., Koch et al. 2014, 2018), we suggest that

the importance of the magnetic field in the process of high-mass star formation depends on the size scales traced and the evolutionary stage of the observed region.

Facility: ALMA.

Software: CASA (v5.1.1, 5.5; McMullin et al. 2007).

Appendix A
Properties from Dust Continuum Emission

The total gas mass can be calculated from the dust emission, in the optically thin limit, as

$$M = \mathbb{R} \, \frac{F_\nu D^2}{\kappa_\nu B_\nu(T)} \, , \qquad (A1)$$

where F_ν is the source flux density, $\mathbb{R}$ is the gas-to-dust mass ratio, D is the distance to the source, κ_ν is the dust opacity per gram of dust, and B_ν is the Planck function at the dust temperature T. Assuming a dust-to-gas mass ratio of 100, dust opacity of 1.03 cm^2 g^{-1} (interpolated to 1.2 mm assuming $\beta = 1.6$; Ossenkopf & Henning 1994), and a temperature of 30 K (Lu et al. 2014), the computed total mass is 75 $M_\odot$. The number density, $n(H_2) = M/(\text{Volume} \times \mu_{H_2} m_H)$ with μ_{H_2} the molecular weight per hydrogen molecule and m_H the hydrogen mass, and the surface density, $\Sigma = M/(\pi \, r^2)$, can be calculated assuming a spherical core. We define an effective radius ($r_{\rm eff}$) determined by the area (A) emitting above 10σ as $r_{\rm eff} = (A/\pi)^{1/2}$, resulting in $r_{\rm eff} = 2\farcs36$ (equal to 0.027 pc or 5500 au). Assuming $\mu_{H_2} = 2.8$, we obtain an $n(H_2)$ of 1.3×10^7 cm^{-3} and $\Sigma = 6.9$ g cm^{-2}, values characteristic of cores forming high-mass stars. The free-fall time is determined from

$$t_{\rm ff} = \sqrt{\frac{3\pi}{32 G \rho}} \, , \qquad (A2)$$

where G is the gravitational constant and ρ is the mass density, $n(H_2) \times \mu_{H_2} m_H$. With ρ equal to 6.3×10^{-17} g cm^{-3}, the free-fall time is 8.4×10^3 yr.

Appendix B
Properties from Line Emission

We estimated the total gas mass in the spiral-like feature and filaments from the H^{13}CO$^+$ emission following a standard procedure (Sanhueza et al. 2012) as follows. First, the column density for a linear, rigid rotor in the optically thin regime, assuming a filling factor of unity, can be calculated from

$$N = \frac{3k}{8\pi^3 B_{\rm rot} \mu^2} \frac{(T_{\rm ex} + hB_{\rm rot}/3k_B)}{(J+1)} \frac{\exp(E_J/kT_{\rm ex})}{[1 - \exp(-h\nu/kT_{\rm ex})]}$$
$$\times \frac{1}{[J(T_{\rm ex}) - J(T_{\rm bg})]} \int T_b \, dv \, ,$$
$$\qquad (B1)$$

where k_B is the Boltzmann constant, h is the Planck constant, $T_{\rm ex}$ is the excitation temperature (30 K; Lu et al. 2014), ν is the transition frequency (260.255339 GHz), μ is the permanent dipole moment of the molecule (3.89 D), J is the rotational quantum number of the lower state, $E_J = hB_{\rm rot}J(J+1)$ is the energy in the level J, $B_{\rm rot}$ is the rotational constant of the molecule (43.377302 GHz), T_b is the brightness temperature, $T_{\rm bg}$ the background temperature, and $J(T)$ is defined as

$$J(T) = \frac{h\nu}{k} \frac{1}{e^{h\nu/kT} - 1} \, . \qquad (B2)$$

The column density is then converted into mass using

$$M = \left[\frac{H^{13}CO^+}{H_2} \right]^{-1} \mu_{H_2} A \sum N(H^{13}CO^+) \, , \qquad (B3)$$

where A is the size of the emitting area in an individual position (pixel of 0.05″), [H^{13}CO$^+$/H$_2$] is the H^{13}CO$^+$ to molecular hydrogen abundance ratio, and the sum is over all the observed positions. We have assumed an [H^{13}CO$^+$/H$_2$] abundance ratio typical of high-mass star-forming regions equal to 1.28×10^{-10} (Hoq et al. 2013).

Appendix C
Magnetic Field Modeling

The idealized model used represents a cloud in magnetostatic equilibrium with density and magnetic field strength decreasing with radius as r^{-2} and r^{-1}, respectively. The field lines are spirals wrapping around nested hourglass-shaped magnetic flux tubes, and have a kink in the equatorial plane where the toroidal component changes sign. The parameters of the model are (i) the mass-to-magnetic-flux ratio normalized to its critical value, λ, given by

$$\lambda = \frac{(M/\Phi_B)}{(M/\Phi_B)_{\rm cr}} = 2\pi G^{1/2} \frac{M}{\Phi_B} \, , \qquad (C1)$$

where G is the gravitational constant, M is the core mass, and Φ_B is the magnetic flux; (ii) the ratio of the strength of the toroidal and poloidal magnetic field components in the midplane, b_0; and (iii) the inclination of the toroid with respect to the plane of the sky, i ($i = 0$ for face-on). The latter is assumed positive if the magnetic field in the north side is directed toward the observer. In principle the orientation of the projection of the magnetic axis on the plane of the sky, φ, should also be considered as a further parameter, but as we will show, the best-fit model indicates that the equatorial plane of
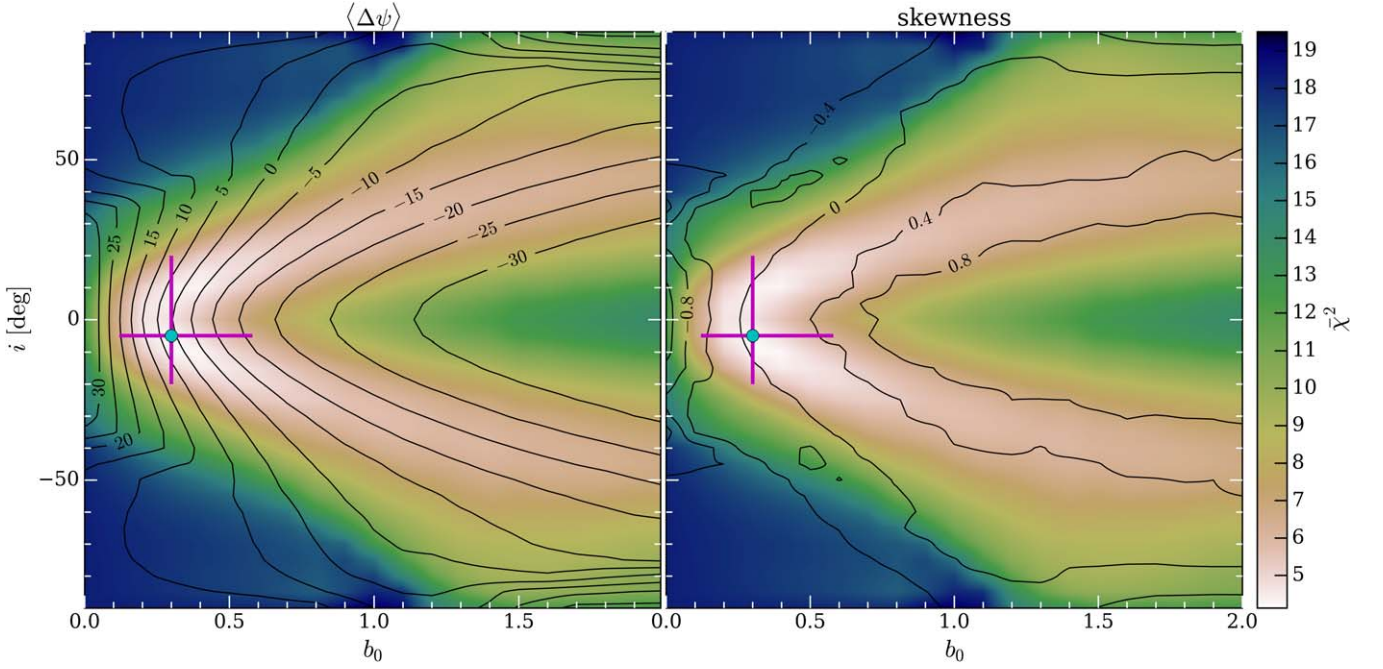
Figure 5. Map of the $\bar{\chi}^2$ distribution of residuals as a function of the inclination, i, and the toroidal-to-poloidal ratio, b_0, for the model with $\lambda = 8.38$. The black isocontours show the average value of the polarization angle residuals $\Delta\psi = \psi_{\mathrm{obs}} - \psi_{\mathrm{mod}}$ (left panel) and the skewness (also known as moment 3) of their distribution (right panel). The solid cyan circle and the magenta lines show the best-fit values of b_0 and i and their uncertainties, respectively.

the cloud is practically in the plane of the sky ($i = -5°$), so that the model turns out to be insensitive to φ.

We considered four values for λ. The extreme cases include a nearly spherical density profile with a weak magnetic field ($\lambda = 16.2$) and a flat density profile with a strong magnetic field ($\lambda = 1.63$). The two intermediate cases correspond to $\lambda = 2.66$ and 8.38. For the magnetic field configuration, we have considered the range of b_0 from the pure poloidal case ($b_0 = 0$) to the case where the strength of the toroidal component is twice the poloidal one ($b_0 = 2$). Finally, we have taken inclinations with respect to the plane of the sky between $-90°$ and $90°$.

The lowest χ^2 value, 4.13, is found for the set $\lambda = 8.38$, $b_0 = 0.30^{+0.28}_{-0.18}$, and $i = -5^{+25°}_{-15}$ (uncertainties on b_0 and i have been estimated using the method of Lampton et al. 1976). The best-fit model can be seen in Figure 4. For completeness, Figure 5 shows the map of the $\bar{\chi}^2$ distribution as a function of the explored range of b_0 and i. Superimposed on this map are the isocontours of the average value of the polarization angle residuals, $\langle\Delta\psi\rangle$ (left panel), and the skewness (also known as moment 3) parameter of their distribution (right panel). The mass-to-magnetic-flux ratio that corresponds to the minimum $\bar{\chi}^2$ also gives the distribution of $\Delta\psi$ with the smallest degree of skewness (equal to 0.12, namely, the distribution is only slightly positively skewed, which means that the peak of the distribution is shifted toward negative values as seen in the inset of Figure 4).

Appendix D
Magnetic Field Properties and Energy Balance

The magnitude of the magnetic field was estimated using the DCF method, following the procedure of Beltrán et al. (2019)

$$B_{\mathrm{pos}} = \xi \frac{\sigma_{\mathrm{los}}}{\delta\psi_{\mathrm{int}}} \sqrt{4\pi\rho} , \qquad (D1)$$

where $\xi = 0.5$ is a correction factor derived from turbulent cloud simulations (Ostriker et al. 2001) and σ_{los} is the line-of-sight velocity dispersion. The DCF method assumes that σ_{los} is from turbulence, and indeed, the observed velocity dispersion is 2.6 times the thermal line width. The average velocity dispersion (σ_{los}) for both $H^{13}CO^+$ velocity components above the 10σ area, in the continuum image, is 0.75 km s^{-1} (both blueshifted and redshifted components have practically the same line width). The density used in the estimation of the magnetic field strength is 6.3×10^{-17} g cm^{-3}. $\delta\psi_{\mathrm{int}}$ is the intrinsic angle dispersion given by $\delta\psi_{\mathrm{int}} = (\sigma_\psi^2 - \delta\psi_{\mathrm{obs}}^2)^{1/2}$. σ_ψ of $18°.1$ is the standard deviation of the polarization angle residuals obtained from the magnetic field modeling (see inset in Figure 4, top), and $\delta\psi_{\mathrm{obs}}$ of $6°.0$ is the mean angle uncertainty in the whole debiased polarization angle image. The derived $\delta\psi_{\mathrm{int}}$ of $17°.1$ results in a magnetic field strength of $B_{\mathrm{pos}} = 3.5$ mG. The Alfvén speed, given by $\sigma_A = B/\sqrt{4\pi\rho}$, is 1.26 km s^{-1}.

We calculate the mass-to-magnetic-flux ratio normalized to the critical value, λ, using Equation (C1) and the fact that $\Phi_B = B\pi R^2$. Adopting $R = r_{\mathrm{eff}}$, we obtain a value of λ equal to 3.2.

The ratio of the turbulent to magnetic energy, β_t, is given by

$$\beta_t = 3\left(\frac{\sigma_{\mathrm{los}}}{\sigma_A}\right)^2 . \qquad (D2)$$

The calculated β_t is 1.07, which indicates that turbulence and the magnetic field play a comparable role in the energy budget of the system.

We assess the importance of the rotational energy with respect to gravity and the magnetic field as follows. First, we

take the ratio between the gravitational energy, E_G,

$$E_G = -\frac{GM^2}{R}\left(\frac{3-\alpha}{5-2\alpha}\right), \tag{D3}$$

and the rotational energy, E_{rot},

$$E_{rot} = \frac{1}{2}I\Omega^2 = \frac{1}{3}Mv_{rot}^2\left(\frac{3-\alpha}{5-\alpha}\right), \tag{D4}$$

where the moment of inertia (I) of a sphere has been assumed, the angular velocity is given by $\Omega = v_{rot}/R$, v_{rot} is the rotational velocity, and α corresponds to the exponent in a density profile of the form $\rho(R) \propto R^{-\alpha}$ (where $\alpha = 0$ implies a uniform density profile and $\alpha = 2$ a centrally peaked density profile; Belloche 2013). The maximum velocity gradient observed is of 2 km s^{-1}. If we assume as the upper limit that this gradient is purely produced by rotation, we obtain a E_{rot}/E_G ratio of 0.11 for a uniform density profile ($\alpha = 0$) and 0.037 for a centrally peak density profile ($\alpha = 2$).

To evaluate the relative importance between rotation and the magnetic field, we follow two approaches: the rotation-to-magnetic-field-energy ratio and the prescription from Machida et al. (2005). First, the energy in the magnetic field (E_B) is given by

$$E_B = \frac{1}{8\pi}B^2V = \frac{1}{6}B^2R^3, \tag{D5}$$

where V is the volume, assumed here to be a sphere. Taking into account the same consideration from above (velocity gradient entirely produced by rotation), the E_{rot}/E_B ratio is 1.0 for a uniform density distribution and 0.56 for a centrally peaked density distribution. These results suggest that the magnetic field is slightly more important than rotation, depending on the exact density profile.

Second, for assessing whether the magnetic field dominates over rotation during the collapse of clouds, Machida et al. (2005) suggest that the ratio of the angular velocity to the magnetic flux density can be used. According to the following relation, if the observed ratio is

$$\left(\frac{\Omega}{B}\right)_{obs} > 0.39\frac{\sqrt{G}}{\sigma_{th}}$$
$$= 1.69 \times 10^{-7} \times \left(\frac{\sigma_{th}}{0.19 \text{ km s}^{-1}}\right)^{-1} \text{yr}^{-1} \mu G^{-1}, \tag{D6}$$

rotation dominates over the magnetic field; otherwise, the magnetic field dominates over rotation. Evaluating the thermal velocity dispersion (isothermal sound speed), $\sigma_{th} = \left(\frac{k_BT}{\mu m_H}\right)^{1/2}$, for a temperature of 30 K and using the mean molecular weight per free particle $\mu = 2.37$, we obtain the right-hand side of Equation (D6) equal to 9.8×10^{-8} yr^{-1} μG^{-1}. Evaluating the observed ratio, we obtain 2.2×10^{-8} yr^{-1} μG^{-1}. The observed ratio is lower than the right-hand side of Equation (D6) by a factor 4.5, suggesting that from this analysis the magnetic field dominates over rotation. Based on both methods employed to assess the importance of rotation with respect to the magnetic field, we conclude that the magnetic field is slightly more important than rotation.

The dynamical state of cores is generally evaluated by using the virial theorem. The ratio between the virial mass, M_{vir}, and the total mass defines the virial parameter, α_{vir}. A virial parameter of unity implies equilibrium, $\alpha_{vir} < 1$ implies gravitational collapse, and $\alpha_{vir} > 1$ means the core is expanding and it will disperse. In its simplest form, the virial analysis only includes gravity and the kinetic energy (turbulence and thermal energy) as follows:

$$\alpha_{vir} = \frac{M_{vir}}{M} = 3\left(\frac{5-2\alpha}{3-\alpha}\right)\frac{R\sigma_{los}^2}{GM}, \tag{D7}$$

resulting in $\alpha_{vir} = 0.24$ for a uniform density profile ($\alpha = 0$) and 0.14 for a centrally peaked density profile ($\alpha = 2$). Both low α_{vir} values, in the absence of other energies, indicate that the core is collapsing dominated by gravity.

The virial parameter considering the magnetic field, is written as follows (e.g., Sanhueza et al. 2017):

$$\alpha_{vir,B} = \frac{M_{vir}}{M} = 3\left(\frac{5-2\alpha}{3-\alpha}\right)\frac{R}{GM}\left(\sigma_{los}^2 + \frac{\sigma_A^2}{6}\right), \tag{D8}$$

which results in $\alpha_{vir,B}$ of 0.35 for a uniform density profile and 0.21 for a centrally peaked density profile. Including the magnetic field, gravity continues to be dominant and the core is collapsing.

We derive the contribution of rotation in the virial equation as below. The virial theorem can be written as

$$\frac{1}{2}\frac{d^2I}{dt^2} = 2E_k + E_G + E_B,$$
$$= 2(E_{n-rot} + E_{rot}) + E_G + E_B, \tag{D9}$$

in which E_k is the kinetic energy that can be separated in a rotational part (E_{rot}) and nonrotational part (E_{n-rot}; McKee & Zweibel 1992). The nonrotational part includes thermal and turbulent energies as follows:

$$E_{n-rot} = \frac{3}{2}M\sigma_{los}^2, \tag{D10}$$

where the observed velocity dispersion is $\sigma_{los}^2 = \sigma_{th}^2 + \sigma_{tur}^2$ and σ_{tur} is the turbulent component. E_{n-rot} is frequently assumed as E_k when rotation is neglected. In virial equilibrium, the moment of inertia does not vary over time and the left-hand side of Equation (D9) becomes zero. Solving Equation (D9) for the mass, one can find the virial mass and the virial parameter can be calculated. If rotation and magnetic energies are ignored, Equation (D7) is recovered. If only rotation is ignored, Equation (D8) is found. Solving for all energies in play, we obtain

$$\alpha_{vir,B,rot} = 3\left(\frac{5-2\alpha}{3-\alpha}\right)\frac{R}{GM}$$
$$\times \left(\sigma_{los}^2 + \frac{\sigma_A^2}{6} + \frac{2}{9}\left(\frac{3-\alpha}{5-\alpha}\right)v_{rot}^2\right). \tag{D11}$$

For a uniform density profile and for a centrally peaked density distribution, we obtain virial parameters of 0.57 and 0.28, respectively. This implies that at the scales we probe with our ALMA observations, even when both the magnetic field and rotation are considered, gravity is still the dominant dynamical force (independently of the density profile assumed).

ORCID iDs

Patricio Sanhueza ⓘ https://orcid.org/0000-0002-7125-7685
Josep Miquel Girart ⓘ https://orcid.org/0000-0002-3829-5591
Marco Padovani ⓘ https://orcid.org/0000-0003-2303-0096
Daniele Galli ⓘ https://orcid.org/0000-0001-7706-6049
Charles L. H. Hull ⓘ https://orcid.org/0000-0002-8975-7573
Qizhou Zhang ⓘ https://orcid.org/0000-0003-2384-6589
Paulo Cortes ⓘ https://orcid.org/0000-0002-3583-780X
Ian W. Stephens ⓘ https://orcid.org/0000-0003-3017-4418
Manuel Fernández-López ⓘ https://orcid.org/0000-0001-5811-0454
James M. Jackson ⓘ https://orcid.org/0000-0002-3466-6164
Benjamin Wu ⓘ https://orcid.org/0000-0003-3874-7030
Luis A. Zapata ⓘ https://orcid.org/0000-0003-2343-7937
Fernando Olguin ⓘ https://orcid.org/0000-0002-8250-6827
Xing Lu ⓘ https://orcid.org/0000-0003-2619-9305
Andrea Silva ⓘ https://orcid.org/0000-0001-9500-604X
Ya-Wen Tang ⓘ https://orcid.org/0000-0002-0675-276X
Takeshi Sakai ⓘ https://orcid.org/0000-0003-4521-7492
Andrés E. Guzmán ⓘ https://orcid.org/0000-0003-0990-8990
Ken'ichi Tatematsu ⓘ https://orcid.org/0000-0002-8149-8546
Fumitaka Nakamura ⓘ https://orcid.org/0000-0001-5431-2294
Huei-Ru Vivien Chen ⓘ https://orcid.org/0000-0002-9774-1846

References

Belloche, A. 2013, in Role and Mechanisms of Angular Momentum Transport During the Formation and Early Evolution of Stars, EAS Publications Series, Vol. 62, ed. P. Hennebelle & C. Charbonnel (Les Ulis: EDP Sciences), 25
Beltrán, M. T., Padovani, M., Girart, J. M., et al. 2019, A&A, 630, A54
Beuther, H., Hunter, T. R., Zhang, Q., et al. 2004a, ApJL, 616, L23
Beuther, H., Soler, J. D., Linz, H., et al. 2020, ApJ, 904, 168
Beuther, H., Vlemmings, W. H. T., Rao, R., & van der Tak, F. F. S. 2010, ApJL, 724, L113
Beuther, H., Zhang, Q., Hunter, T. R., et al. 2004b, ApJL, 616, L19
Chandrasekhar, S., & Fermi, E. 1953, ApJ, 118, 116
Clark, S. E., Peek, J. E. G., & Putman, M. E. 2014, ApJ, 789, 82
Contreras, Y., Sanhueza, P., Jackson, J. M., et al. 2018, ApJ, 861, 14
Cortes, P. C., Hull, C. L. H., Girart, J. M., et al. 2019, ApJ, 884, 48
Cortes, P. C., Le Gouellec, V. J. M., Hull, C. L. H., et al. 2021, ApJ, 907, 94
Cortes, P. C., Sanhueza, P., Houde, M., et al. 2021, ApJ, submitted
Dall'Olio, D., Vlemmings, W. H. T., Surcis, G., et al. 2017, A&A, 607, A111
Davis, L. 1951, PhRv, 81, 890
Fernández-López, M., Sanhueza, P., Zapata, L. A., et al. 2021, ApJ, 913, 29
Fissel, L. M., Ade, P. A. R., Angilè, F. E., et al. 2019, ApJ, 878, 110
Girart, J. M., Beltrán, M. T., Zhang, Q., Rao, R., & Estalella, R. 2009, Sci, 324, 1408
Goddi, C., Ginsburg, A., Maud, L. T., Zhang, Q., & Zapata, L. A. 2020, ApJ, 905, 25
Hoq, S., Jackson, J. M., Foster, J. B., et al. 2013, ApJ, 777, 157
Hull, C. L. H., Cortes, P. C., Gouellec, V. J. M. L., et al. 2020, PASP, 132, 094501
Hull, C. L. H., Mocz, P., Burkhart, B., et al. 2017, ApJL, 842, L9
Hull, C. L. H., & Zhang, Q. 2019, FrASS, 6, 3
Izquierdo, A. F., Galván-Madrid, R., Maud, L. T., et al. 2018, MNRAS, 478, 2505
Juvela, M., Guillet, V., Liu, T., et al. 2018, A&A, 620, A26
Koch, P. M., Tang, Y.-W., Ho, P. T. P., et al. 2014, ApJ, 797, 99
Koch, P. M., Tang, Y.-W., Ho, P. T. P., et al. 2018, ApJ, 855, 39
Lampton, M., Margon, B., & Bowyer, S. 1976, ApJ, 208, 177
Li, Z.-Y., & Shu, F. H. 1996, ApJ, 472, 211
Liu, H. B., Galván-Madrid, R., Jiménez-Serra, I., et al. 2015, ApJ, 804, 37
Liu, T., Li, P. S., Juvela, M., et al. 2018, ApJ, 859, 151
Lu, X., Zhang, Q., Liu, H. B., et al. 2018, ApJ, 855, 9
Lu, X., Zhang, Q., Liu, H. B., Wang, J., & Gu, Q. 2014, ApJ, 790, 84
Machida, M. N., Matsumoto, T., Tomisaka, K., & Hanawa, T. 2005, MNRAS, 362, 369
Maud, L. T., Hoare, M. G., Galván-Madrid, R., et al. 2017, MNRAS, 467, L120
McKee, C. F., & Zweibel, E. G. 1992, ApJ, 399, 551
McMullin, J. P., Waters, B., Schiebel, D., Young, W., & Golap, K. 2007, in ASP Conf. Ser., 376, Astronomical Data Analysis Software and Systems XVI, ed. R. A. Shaw, F. Hill, & D. J. Bell (San Francisco, CA: ASP), 127
Olguin, F. A., Sanhueza, P., Guzmán, A. E., et al. 2021, ApJ, 909, 199
Ossenkopf, V., & Henning, T. 1994, A&A, 291, 943
Ostriker, E. C., Stone, J. M., & Gammie, C. F. 2001, ApJ, 546, 980
Padovani, M., Brinch, C., Girart, J. M., et al. 2012, A&A, 543, A16
Padovani, M., & Galli, D. 2011, A&A, 530, A109
Padovani, M., Hennebelle, P., & Galli, D. 2013, A&A, 560, A114
Palmeirim, P., André, P., Kirk, J., et al. 2013, A&A, 550, A38
Planck Collaboration, Ade, P. A. R., Aghanim, N., et al. 2016, A&A, 586, A138
Sanhueza, P., Jackson, J. M., Foster, J. B., et al. 2012, ApJ, 756, 60
Sanhueza, P., Jackson, J. M., Zhang, Q., et al. 2017, ApJ, 841, 97
Soam, A., Liu, T., Andersson, B. G., et al. 2019, ApJ, 883, 95
Soler, J. D., Ade, P. A. R., Angilè, F. E., et al. 2017, A&A, 603, A64
Sridharan, T. K., Beuther, H., Schilke, P., Menten, K. M., & Wyrowski, F. 2002, ApJ, 566, 931
Tobin, J. J., Hartmann, L., Bergin, E., et al. 2012, ApJ, 748, 16
Vaillancourt, J. E. 2006, PASP, 118, 1340
Vlemmings, W. H. T. 2008, A&A, 484, 773
Xu, Y., Moscadelli, L., Reid, M. J., et al. 2011, ApJ, 733, 25
Zapata, L. A., Rodríguez, L. F., Ho, P. T. P., Beuther, H., & Zhang, Q. 2006, AJ, 131, 939
Zhang, Q., Qiu, K., Girart, J. M., et al. 2014, ApJ, 792, 116